

Development of Insect Thorax Based Flapping Mechanism.

Zaem Khan, Kyle Steelman and Sunil Agrawal

Abstract—Design of a flapping mechanism for flapping wing micro air vehicles (FWMAV) is presented based on a mathematical model of insect thorax. This model also includes an aerodynamic model of flapping wings. Using experiments on dynamically scaled wings and numerical optimization, the mechanism is tuned for peak aerodynamic performance. The thorax model is used to understand the mechanics of the biological flapping mechanism and reveals the significance of rotational stiffness and inertia distribution in flapping wings. Experiments conducted on the actual thorax based mechanism validate theoretical findings and also show significant lift generation capability.

I. INTRODUCTION

Flapping wing micro Air vehicles (FWMAVs) represent an emerging class of aerial vehicles that can be used for numerous applications that include searching for survivors in burning buildings and under collapsed structures, sensing of chemical leaks in industry, detection of radiations in nuclear plants as well as surveillance and reconnaissance. Inspired by the sophisticated biological designs of insects and hummingbirds, FWMAVs are expected to show similar aerial maneuverability. Recent success of micro scale robotic insect experiment brings us closer to achieving this goal [13].

In the quest for developing FWMAV, engineers have focused on the design of flapping mechanisms for generating insect-like wing motion [7], [8]. Typically, this involves optimizing the parameters of the mechanism with the aim to minimize the error between the generated motion and a given insect-like wing motion. However, the main difficulty lies in the implementation of the design at FWMAV scale due to the impact loads of the beating wings near the end of the stroke caused by high flapping frequency. The impacts waste energy in noise and require strength in the mechanism, which adds weight and renders the design incapable of flight. Furthermore, mimicking insect wing motion does not guarantee peak aerodynamic performance [1]. Therefore, this approach reveals a disconnect between the optimal aerodynamic performance and mechanism design.

In our work, we develop a simplified mathematical model of insect thorax which allows elastic storage of energy. Computer simulations of the model show insect-like wing motion including passive flip. we conduct aerodynamic

tests on dynamically scaled wings to determine the optimal kinematics. The optimal kinematics is then related to the parameters of the thorax-model in order to ‘tune’ it for the peak aerodynamic performance. The thorax model is used as a basis for the design of a flapping mechanism. This design mimics the mechanics of the insect thorax actuation rather than the insect wing motion. Micro DC motor (typically used in model aircraft) is used to power the mechanism.

II. MODEL OF INSECT THORAX

The insect thorax consists of a highly elastic exoskeleton containing flight muscles. These muscles contract alternately and move the tergal plate which causes the wings to flap through a hinge mechanism as shown in Fig. 1A and B. As the wings approach the end of each stroke, the kinetic energy of the wing is stored as strain energy due to the deformation of the thorax shown shaded in Figs. 1A and B. We denote the flap angle by θ_f while θ_e is the excitation angle or the flap angle assuming no deformation of thorax exoskeleton. The difference $\theta_f - \theta_e$ results in storage of strain energy. As the wing flaps, it twists passively along the span at the end of each stroke due to the aerodynamic and inertial loads as shown in Fig. 1C. The remarkable design of insect wing structure prevents the wing from twisting beyond an optimal angle of attack α^* [14]. The rotational stiffness increases sharply and maintains α^* during the flapping phase of the motion.

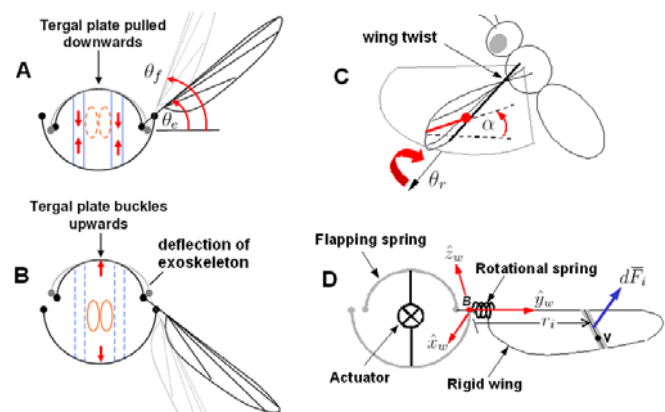


Fig. 1. Schematic showing the working of insect thorax mechanism and a simplified model to capture its essential mechanics.

We model the thorax flapping mechanism by replacing the thorax flight muscles by an actuator, which provides the excitation as shown in Fig. 1D. The tergal plate and the elastic wing twist at the wing base are modeled by

This work is supported by National Science Foundation
Zaem Khan is a doctoral candidate in BIOMS/Mechanical Engineering Program at University of Delaware, Newark, DE, 19716 zaem@udel.edu

Kyle Steelman is an undergraduate student in Department of Mechanical Engineering, University of Delaware, Newark, DE, 19716, USA Kyle@udel.edu

Dr. Sunil Agrawal is a Faculty in Mechanical Engineering, University of Delaware, Newark, DE, 19716, USA agrawal@udel.edu

nonlinear springs. The wing is assumed to be rigid which undergoes flapping and rotational motions denoted by the angles θ_f and θ_r respectively. We attach a coordinate frame $\mathcal{F}_w : (\hat{x}_w, \hat{y}_w, \hat{z}_w)$ to the rigid wing as shown in Fig. 1D with the origin denoted by B at the wing base. The \hat{x}_w axis is normal to the wing surface, \hat{y}_w axis is in the spanwise direction along the wing leading edge and \hat{z}_w is along the chordwise direction.

A. Equations of motion

The equations of motion of the system are given below

$$M(q)\ddot{q} + C(q, \dot{q}) + G(q) = Q, \quad (1)$$

where $q = (\theta_f, \theta_r)^T$ and

$$\begin{aligned} M(q) &= \begin{pmatrix} \sin^2 \theta_r J_x + \cos^2 \theta_r J_z & \cos \theta_r J_{yz} \\ \cos \theta_r J_{yz} & J_y \end{pmatrix}, \\ C(q, \dot{q}) &= \begin{pmatrix} (J_x - J_z) \sin(2\theta_r) \dot{\theta}_f \dot{\theta}_r - J_{yz} \sin \theta_r \dot{\theta}_r^2 \\ -\frac{1}{2} (J_x - J_z) \sin(2\theta_r) \dot{\theta}_f^2 \end{pmatrix}, \\ G(q) &= \begin{pmatrix} -K_{f1}(\theta_e - \theta_f) - K_{f2}(\theta_e - \theta_f)^3 \\ K_{r1}\theta_r + K_{r2}\theta_r^3 + K_{r3}\theta_r \end{pmatrix}, \\ Q(q, \dot{q}) &= \begin{pmatrix} -\cos \theta_r \sum_{i=1}^N r_i dF_i \\ -0.5 \sum_{i=1}^N c_i dF_i - \mu_r \dot{\theta}_r \end{pmatrix}, \end{aligned}$$

where J_x , J_z and J_{yz} are the wing moments and product of inertia in \mathcal{F}_w frame, $\theta_e = \Theta_e \cos \omega_e t$ is the sinusoidal excitation angle where Θ_e is the excitation amplitude and ω_e is the excitation frequency. K_{f1} , K_{f2} are the parameters of the flapping spring and K_{r1} , K_{r2} , K_{r3} are parameters of the rotational spring, μ_r is the viscous damping coefficient about the rotational axis. The parameter K_{r3} models the sharp increase in rotational stiffness which locks the wing at the optimal angle of attack α^* during the flapping phase. $K_{r3} = 0$ if $|\theta_r| < \theta_r^*$ and non-zero if $|\theta_r| \geq \theta_r^*$. Where θ_r^* equals $\pi/2 - \alpha^*$. For the lock to take effect, $K_{r3} \gg K_{r1}, K_{r2}$.

B. Aerodynamic model

The aerodynamic force on flapping wings is normal to the wing surface due to dominance of pressure force [10]. It can be modeled using blade element method (BEM) in which the wing is divided into N elements. For the i^{th} element, located at a distance r_i from the wing base B having a cord c_i and width dr_i , the differential normal force is given by

$$d\bar{F}_i = dF_i \hat{x}_w = \left(C_1(\alpha_i) \frac{\rho}{2} |\bar{V}_i|^2 c_i dr_i \right) \hat{x}_w, \quad (2)$$

where $\bar{V}_i = V_{ix} \hat{x}_w + V_{iz} \hat{z}_w$ is the flow velocity vector (V_{iy} component does not contribute to the aerodynamic force), $C_1(\alpha_i)$ is a coefficient of normal force which is a function of angle of attack α_i of the i^{th} element and ρ is the density of air. Based on a model by Walker [11], the rotational force peaks are modeled by computing \bar{V}_i at a location 'v' along the chord at each blade element as shown in Fig. 1D. Further details about the aerodynamic model can be found in [5].

C. Computer Simulation

The dynamic equation (1) along with the aerodynamic model given by (2) constitutes the complete model of the system. The numerical simulation of this system after reaching steady-state is shown in Fig. 2. The motion is qualitatively similar to the insect wing motion [1]. The flapping motion is nearly sinusoidal while the rotational motion is trapezoidal and marked by overshoots after the wing flips. Note that θ_r varies very little from θ_r^* during the flapping phase due to the presence of K_{r3} term. The insect-like kinematics can be described by a few parameters which allow variation in kinematics without changing it qualitatively. These are the stroke amplitude ' Θ_f ', the constant angle of attack $\alpha^* = \pi/2 - \theta_r^*$, the phase ' ϕ_r ' between the flapping and rotational motion and the duration of rotation ' ΔT ' which is a fraction of wing beat time period ' T ' during which flip occurs [9].

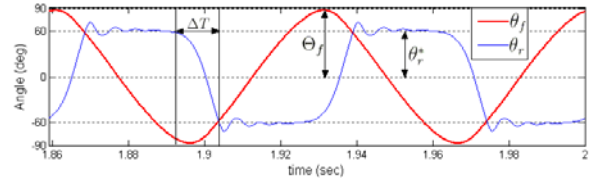


Fig. 2. shows the numerical simulation of (1) after reaching steady-state. $\Theta_f \approx 90^\circ$ and $\theta_r^* = 60^\circ$ or $\alpha^* = \pi/2 - \theta_r^* = 30^\circ$.

III. OPTIMAL HOVERING KINEMATICS

We now determine the optimal set of kinematic parameters, described above, which maximize the aerodynamic performance. We will then tune the thorax model to obtain the optimal kinematics. In the past, experiments have been conducted to determine the optimal kinematics using dynamically scaled fruit-fly wings at a Reynolds number range of 100-200 [9]. However, aerodynamic data of flapping wings is not available in a Reynolds number (Re) range of 10,000 to 20,000, which is the expected operating range of a hummingbird sized FWMAV. To characterize the optimal kinematics at this Re , we conducted our own aerodynamic tests using a robotic flapping wing device shown in Fig. 3.

The flapper provides the (θ_f, θ_r) motion. The force and torque data from the sensor is filtered online using a first-order filter and offline with a zero-phase delay low-pass Butterworth filter with a cut-off frequency set to 15 times the flapping frequency. The gravity and inertial loads are computed online using Newton-Euler equations of the rigid wing and subtracted from the sensor output to get the pure aerodynamic loads. This data is in the wing frame \mathcal{F}_w as shown in Fig. 3 and transformed into the lift and drag axes which are normal and parallel to the stroke-plane. We used dSpace system for control of flapper motors and data acquisition. To obtain dynamic scaling, the Reynolds number ' Re ' for flapping wings [4] is matched between the flapper wing and a $1/5^{th}$ scale FWMAV wing. The cycle averaged lift, drag and lift coefficient are defined as follows

$$\bar{L} = \frac{1}{T} \int_0^T L(t) dt, \quad \bar{D} = \frac{1}{T} \int_0^T |D(t)| dt, \quad C_L = \frac{\bar{L}}{0.5 \rho S_2 (\pi f \Theta_f)^2} \quad (3)$$

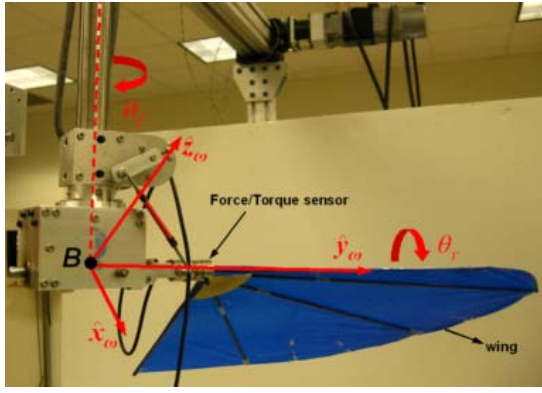


Fig. 3. shows the robotic flapper designed and fabricated at University of Delaware. It is driven by independent servo motors and can generate (θ_f, θ_r) wing motions. A six-axis sensor records the force/torque data generated by the wing. This data is transformed into the wing frame $f_w(\hat{x}_w, \hat{y}_w, \hat{z}_w)$.

where $L(t)$ and $D(t)$ are time varying lift and drag forces, f is the wing beat frequency in Hz, $T = 1/f$ is the cycle period, $S_2 = 2 \sum_i^N c_i dr_i$ is the second moment of wing area [3] and ρ is the density of air. The criteria for aerodynamic performance is high C_L at a high \bar{L}/\bar{D} ratio. Starting from nominal kinematic parameters ($\Theta_f = 30^\circ$, $\alpha^* = 35^\circ$, $\phi_r \equiv 0^\circ$, $\Delta T \equiv \text{nominal}$), we vary each parameter in a sequence of experiments to find the optimal kinematic parameters as follows.

A. Optimal stroke amplitude Θ_f

In the first experiment, Θ_f is varied from 30° to 90° in 10° increments while keeping the product $f\Theta_f$ constant. This ensures constant Re and the denominator of C_L . The experimental results presented in Fig. 4 show an increase of \bar{L}/\bar{D} and C_L with Θ_f .

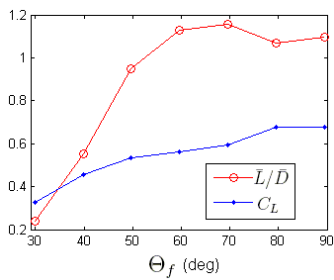


Fig. 4. The effect of varying Θ_f on C_L and \bar{L}/\bar{D} ratio at $Re = 10,263$.

However, by manipulating rotational motion, aerodynamic performance might be improved even for smaller amplitudes. This leads us to the second experiment.

B. Optimal flip motion

In the second experiment, we fix Θ_f at 90° while flip is varied in two ways. (1) ΔT is varied from nominal to fast and slow as shown in Fig. 5A and (2) for each ΔT , the phase ϕ_r is varied from -30° (delayed flip) to 30° (advanced flip) in 5° increments as shown in Fig. 5B.

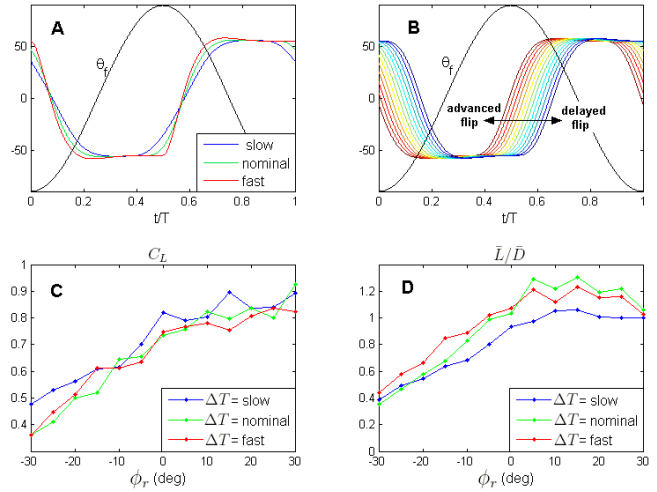


Fig. 5. Effect of variation of flip duration ΔT and phase ϕ_r on C_L and \bar{L}/\bar{D} ratio at $Re = 18,326$.

The experimental results presented in Fig. 5C and D show that advanced flip ($\phi_r > 0^\circ$) results in an increase of C_L as well as \bar{L}/\bar{D} . Maximum \bar{L}/\bar{D} occurs at values of ϕ_r between 0° and 20° while C_L increases almost linearly with ϕ_r . Furthermore, ΔT has very little effect on C_L , however, the nominal and fast flip durations result in an increase in \bar{L}/\bar{D} compared to the slow flip case. Therefore, by manipulating the flip motion, we are able to significantly improve \bar{L}/\bar{D} and C_L at $\Theta_f = 90^\circ$ compared to the data in Fig. 4.

C. Optimal angle of attack α^*

In the above experiments, α^* was maintained at 35° . In this experiment, we fix $\Theta_f = 90^\circ$ and $\Delta T = \text{nominal}$, while α^* is varied from 10° to 70° in 5° increments. The experiment is repeated for five values of ϕ_r ($-5^\circ, 0^\circ, 5^\circ, 10^\circ, 15^\circ$) which includes the optimal range of ϕ_r found in the previous experiment. The results again show that $\phi_r < 0^\circ$ results in a decrease of \bar{L}/\bar{D} and C_L .

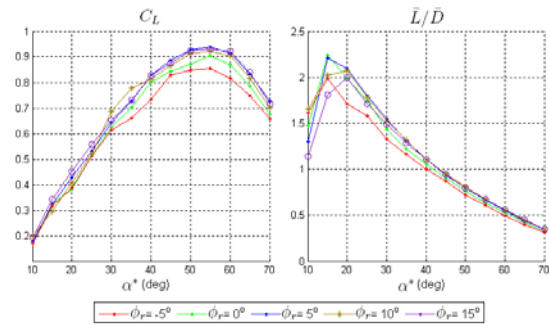


Fig. 6. Effect of variation of α^* on C_L and \bar{L}/\bar{D} ratio at $Re = 18,326$

These results are similar to those obtained in [9]. Based on the last two experiments, we see that maximum \bar{L}/\bar{D} and C_L do not occur at the same parameter values and a compromise must be made. A high C_L is important for carrying payload, whereas a high \bar{L}/\bar{D} reduces aerodynamic power required for a given payload. Based on the requirement for high \bar{L}/\bar{D} ,

the optimal operating point is $\phi_r \approx 10^\circ$, and $\alpha^* \approx 20^\circ$. For high C_L , $\Theta_f = 90^\circ$, $\phi_r = 30^\circ$ and $\alpha^* = 55^\circ$. For both cases, $\Theta_f = 90^\circ$ and $\Delta T = \text{nominal}$.

IV. TUNING THE THORAX MODEL

The parameters of the thorax model can now be related to the optimal kinematic parameters in order to tune the model for peak aerodynamic performance.

A. De-coupling flapping dynamics

The pattern of venation distribution in insect wings shifts the center of mass near the leading edge or \hat{y}_w axis [2]. This means $J_x \approx J_z = J$ and $J_{yz}, J_y \ll J$. The implication of this can be seen if we non-dimensionalize (1) by dividing with J and scaling time by using $\tau = \omega_o t$, where $\omega_o = \sqrt{\frac{K_{f1}}{J}}$. Notice that the coefficient of $\ddot{\theta}_f$ in $M(q)$ becomes one while other terms are much smaller than one. Similarly, the coefficients of terms in $C(q, \dot{q})$ become negligible compared to one. Therefore, flapping dynamics is decoupled from rotational dynamics except for coupling in $Q(q, \dot{q})$. If we assume that the wing maintains optimal α^* during the flapping phase and flips instantaneously ($\Delta T = 0$) without actually rotating, then aerodynamic model is greatly simplified and flapping dynamics is decoupled and given by

$$J\ddot{\theta}_f = K_{f1}(\theta_e - \theta_f) + K_{f2}(\theta_e - \theta_f)^3 - C_a\dot{\theta}|\dot{\theta}| \quad (4)$$

where $C_a = C_1(\alpha^*)\frac{\rho}{2}\cos(\alpha^*)\sum_{i=1}^N r_i^3 c_i dr_i$ is the aerodynamic damping coefficient which is a function of wing geometry and α^* . Therefore, flapping dynamics can be studied independently, however, the rotational dynamics equation remains unchanged in (1) and is highly dependent on flapping dynamics. This result is obvious, since flip occurs passively due to flapping. Based on the results of Fig. 4, maximum Θ_f is desirable. The frequency response (Θ_f vs ω_e) of (4) can be generated numerically to determine the peak amplitude Θ_f^* and ω_e^* at the peak amplitude. At (Θ_f^*, ω_e^*) , we must ensure that $\bar{L} \geq W$ ($W = \text{weight of FWMAV}$) and the average aerodynamic power \bar{P}_a is within the actuator output range. If this is not satisfied, we change the parameters in (4) to increase ω_e^* and Θ_f^* . For constant C_a , increase in stiffness (K_{f1}, K_{f2}) increases ω_e^* while increase in J increases Θ_f^* and decreases ω_e^* . The best way to increase J without increasing the weight or other inertia parameters is to put a mass on the tip of the wing at the leading edge. Some insects, in particular, of the order *odonata* have a concentrated mass called *pterostigma* located precisely in this location as shown in Fig. 7. To verify the significance of pterostigma, we conduct experiments on the actual mechanism in Section VI.

B. Optimal rotational dynamics

Once flapping dynamics given by (4) is tuned at (Θ_f^*, ω_e^*) , we can optimize rotational dynamics to maximize aerodynamic performance. For this purpose, we used numerical optimization based on SQP algorithm available as *fmincon* function in MATLAB. The optimization utilizes, the steady-state solution of (4) (tuned at $\Theta_f^* = 90^\circ$ at $\alpha^* = 25^\circ$) along

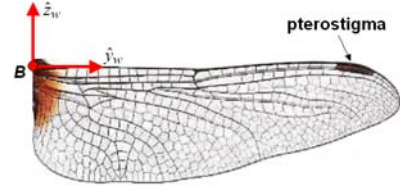


Fig. 7. Figure showing the location of pterostigma on a dragonfly wing.

with the rotational dynamics equation in (1) to generate the cycle averaged \bar{L} and \bar{L}/\bar{D} . The cost function is given by

$$f(K_{r1}, K_{r2}, \delta J_y, \delta J_{yz}, \mu_r) = w_1 \left(\frac{1}{\bar{L}}\right)^2 + w_2 \left(\frac{\bar{D}}{\bar{L}}\right)^2, \quad (5)$$

where w_1, w_2 are weighting coefficients. The cost function is designed to maximize \bar{L} and \bar{L}/\bar{D} . The parameter δJ_y is described as $\delta J_y = (J_y + \Delta J_y)/J_y$, where ΔJ_y is the change in J_y . An increase in J_y gives $\delta J_y > 1$ while a decrease gives $\delta J_y < 1$. No change means $\delta J_y = 1$. Similarly, for the parameter δJ_{yz} . The cost function is subject to the following constraints

$$-K_{r1} < 0, \quad -K_{r2} < 0, \quad -\mu_r < 0, \quad (6)$$

$$0.5 - \delta J_y < 0, \quad \delta J_y - 2 < 0, \quad 0.5 - \delta J_{yz} < 0, \quad \delta J_{yz} - 2 < 0, \quad (7)$$

where the constraints ensure that K_{r1}, K_{r2} , and μ_r remain positive and $\delta J_y, \delta J_{yz}$ are bounded between 0.5 and 2. The quantitative results of optimization can be used to tune the thorax model, however, we are interested in the effect of optimal parameters on aerodynamic performance. Therefore, we generated three rotational motions based on: (1) optimal solution, (2) setting $K_{r1} = K_{r2} = 0$ but other parameters are optimal and (3) $K_{r1} = K_{r2} = 0$ and original (non-optimal) values of J_y and J_{yz} . These three kinematic patterns are used in the robotic flapper to determine the C_L and \bar{L}/\bar{D} . Figure 8 shows the three kinematics and experimental results.

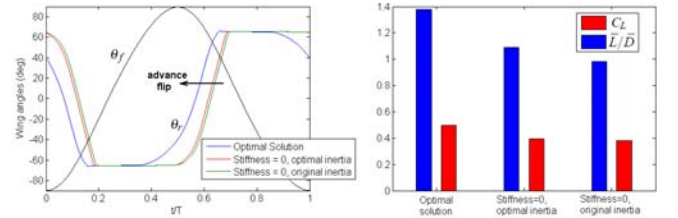


Fig. 8. Experimental results showing the comparison of aerodynamic performance for the three kinematic patterns.

These results clearly shows an increase in aerodynamic performance in the optimal case. Stiffness results in advanced flip compared to the other two cases. As shown in Fig. 5, advanced flip improves aerodynamic performance. Similarly, optimal inertia also results in advanced flip compared to non-optimal case. The optimal solution gives $\delta J_y = 0.5$. This means less mass near the trailing edge of the wing. This

result clearly shows the importance of rotational stiffness and proper inertia distribution in flapping wing aerodynamics.

V. THORAX BASED DESIGN

The model of insect thorax is used as a basis for the design of FWMAV flapping mechanism. In Fig. 9, we present a schematic of a design which does not resemble the insect thorax but mimics its mechanics. In this design, the thorax muscles are replaced by two four-bar linkages driven by a common crank. The rocker is driven through an angle θ_e . The flapping spring connects the wing base to the rocker and the rotational spring connects the wing base to the rigid wing. As the crank rotates by an angle θ_s , power is transmitted to the wing through the flapping spring while flip is generated passively as described by the dynamics of the thorax model.

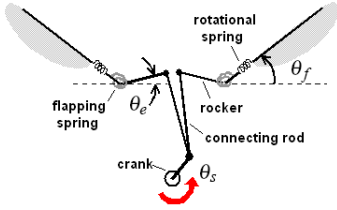


Fig. 9. Schematic showing the working of a flapping mechanism based on the thorax model.

A CAD model of the design is shown in Fig. 10A shows the various components and the assembled wing. The crank is driven by a micro DC motor via a two stage gear reduction. Fig. 10B shows twist in flapping spring of the actual mechanism as the wing is deflected manually. The wing base acts as a bearing for the wing leading edge which can revolve freely until α^* is reached. Rotation beyond α^* is prevented by a locking mechanism shown in Fig. 10C. The rotational spring consists of a rod inserted into the wing base parallel to the wing leading edge. As the wing rotates, the parallel rod is deflected and acts as a rotational spring. The wing is made of carbon rods and covered with Japanese tissue. The pterostigma is a small brass tube which is press fitted at the end of wing leading edge rod and is easily removable. The entire wing assembly is mounted on top of the rocker on a common axle and connected to the rocker through elastic bands. When the wing rotates relative to the rocker, the elastic bands are stretched and act as flapping spring as shown in Fig. 10C. The link lengths of the four-bar mechanism are optimized to achieve a sinusoidal motion with a driving amplitude of $\Theta_e = 30^\circ$ with symmetry between the left and right rocker motions.

VI. EXPERIMENTAL VALIDATION

A. Experimental setup

The key quantities to measure are the cycle average lift \bar{L} and aerodynamic power \bar{P}_a , stroke amplitude Θ_f , and flapping frequency ω_e . The experimental setup used to measure these quantities is shown in Fig. 11. The lift is measured by a weight balance with a resolution of (0.01gmf). The flapping frequency is measured by a stroboscope. To measure Θ_f , we

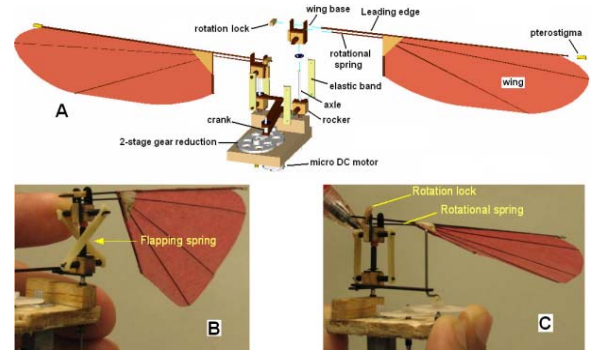


Fig. 10. Figure shows the details of the design. A: CAD model showing the various components, B: Twist in the elastic band flapping spring (actual prototype). C: rotational spring and lock mechanism (actual prototype).

used laser pointers mounted perpendicular to the stroke plane and the table. The pointers illuminate the leading edge of the beating wing at the extremes of the stroke and the point of light also falls on the table and is marked. The angle between the two lines starting from the marked points to the wing rotation axis is $2\Theta_f$ as shown in Fig. 11. This procedure can be repeated over a range of flapping frequencies and allows fairly accurate measurements of Θ_f compared to expensive vision system or encoders which can effect the mechanism dynamics. The stiffness and α^* are measured using custom built tools as shown in Fig. 11 B, C. The inertia parameters are determined from a CAD model of the wing assembly.

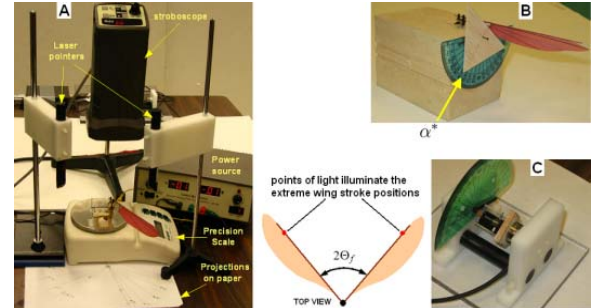


Fig. 11. A: Experimental setup comprising of a stroboscope, laser pointers and a weight balance (0.01 gmf resolution). The schematic shows how Θ_f is measured using light projections. B & C: Custom built tools for measuring and adjusting α^* and spring stiffness.

The micro DC motor is driven by a power source and the voltage V and current I are measured through dspace board. The aerodynamic power can be computed from

$$\bar{P}_a = VI - I^2 R_m - B_s \dot{\theta}_s^2, \quad (8)$$

where VI is the input power to the motor, $I^2 R_m$ is the loss of power in motor windings, $B_s \dot{\theta}_s^2$ is the friction loss of the entire mechanism excluding the wings.

B. Results

We investigated three cases using the same wing. In case A, the wing has rotational stiffness but pterostigma is not used. In case B, pterostigma is included. In case C,

pterostigma is removed as well as the rotational stiffness by cutting the rotational spring rod. This allowed the wing to rotate freely without stiffness upto α^* . The frequency response determined experimentally is shown in Fig. 12 for the three cases along with the frequency response generated by the thorax model using numerical simulation.

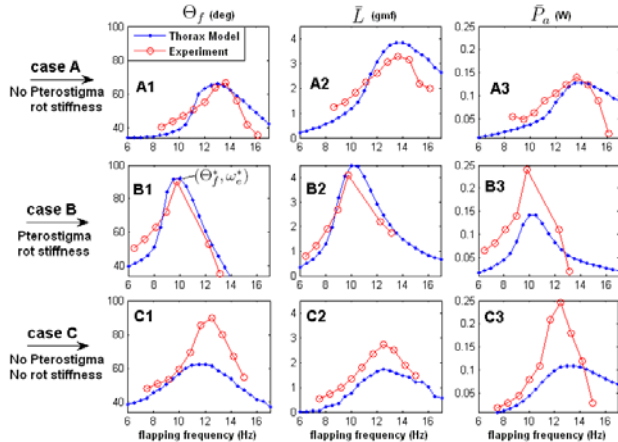


Fig. 12. Figure shows the frequency response of the mechanism in terms of Θ_f , \bar{L} and \bar{P}_a for three cases (plotted in rows). Case A: wing includes rotational stiffness but no pterostigma, case B: same wing with pterostigma and case C: same wing with no rotational stiffness and pterostigma. Experimental data is also compared with the thorax model. In plot B1, (Θ_f^*, ω_e^*) is the point of peak stroke amplitude and frequency.

The experimental data matches very well with the thorax model for cases A and B in terms of the shape of the curves as well as the frequencies at which peak values of Θ_f , \bar{L} and \bar{P}_a occur. Comparison of the plots for cases A and B show that pterostigma increases Θ_f^* and \bar{L} and reduces ω_e^* . However, \bar{P}_a also increases significantly compared to case A and is more than what the thorax-model predicts as shown in plot B3 in Fig. 12. The results of case C should be compared to case A because the only difference is the removal of rotational stiffness in case C. The plots show that removing rotational stiffness results in significant reduction of \bar{L} (compare plots A2 and C2) and significant increase in \bar{P}_a (compare plots A3 and C3). Furthermore, the stroke amplitude is much larger compared to case A (compare plots A1 and C1). However, even with large Θ_f^* , the aerodynamic performance is poor compared to case A. This clearly shows the importance of rotational stiffness in flapping wing flight.

The maximum lift generated is 4.15 gf at roughly 10 Hz using the pterostigma as shown in plot B2. The aerodynamic power required is 0.24 W which is only 16% of the maximum power output (1.5 W) of the motor. The actual FWMAV will require atleast 10 gf of lift per wing. Lift can be increased by increasing flapping frequencies and using α^* for maximum C_L . The required aerodynamic power will also increase, however, we believe that the current motor is powerful enough to cope with the increased power requirements. Furthermore, tiny brushless motors are now available which are much lighter and with a much higher maximum power output.

VII. CONCLUSIONS

In this paper, a 2-DOF model of insect thorax is presented. Computer simulations of the thorax model show insect-like wing kinematics. We have identified the parameters which qualitatively describe the kinematics. Aerodynamic tests revealed the optimal values of these kinematic parameters for peak aerodynamic performance. We also showed that due to the special nature of the inertia distribution, the flapping dynamics can be decoupled from the rotational dynamics while rotational dynamics is highly dependent on flapping dynamics. Therefore, the parameters of the rotational dynamics can only be optimized once the parameters of the flapping dynamics have been found. Using numerical optimization, we found the optimal parameters of the rotational dynamics. Analysis of thorax-model also revealed the importance of rotational stiffness and pterostigma in insect wings. Finally, based on the thorax-model, we presented a design of a flapping mechanism. Experimental evaluation confirmed the role played by rotational stiffness and pterostigma in improving aerodynamic performance. In the future, more tests will be carried out leading to the first prototype FWMAV.

VIII. ACKNOWLEDGMENTS

The authors gratefully acknowledge the funding of National Science Foundation (NSF) in support of this work.

REFERENCES

- [1] Altshuler et al, "Short Amplitude high frequency wing strokes determine the aerodynamics of honeybee flight". *PNAS*, vol. 102, no. 50 1821318218; December 13, 2005
- [2] Robert Dudley, "The biomechanics of insect flight, form, function and evolution." *Princeton University Press*; 2002
- [3] Ellington, C. P. (1984). "The aerodynamics of hovering insect flight. I-V". *Phil. Trans. Royal Society of London B* 305, 115.
- [4] Ellington, C. P. (1999). "The novel aerodynamics of insect flight: applications to micro-air vehicles". *J. Exp. Biol.* 202, 34393448.
- [5] Khan, Z. A., Agrawal, S. K., 2005. "Wing force and moment characterization of flapping wings for micro air vehicle application". *American Control conference*; 2005
- [6] Raney, D. L., Slominski, E. C. "Mechanization and Control concepts for Biologically inspired Micro aerial vehicles". *AIAA guidance, navigation and control conference.*; 2003
- [7] Zbikowski, R., Galinski, C., Pedersen, C. B., Four-Bar Linkage Mechanism for insect-like Flapping Wings in Hover: Concept and an Outline of its Realizations. *Journal of mechanical design*, July 2005, Vol 127.
- [8] Banala, S. K, Agrawal, S. K., Design and Optimization of a Mechanism for Out-of-plane Insect Wing-like Motion With Twist. *Journal of mechanical design*, July 2005, Vol 127.
- [9] Sane, S. P and Dickinson, M. H. "The control of flight force by a Flapping Wing: Lift and Drag Production". *J. Exp. Biol.* 204, 26072626; 2001
- [10] Usherwood, J. R. and Ellington, C. P. "The aerodynamics of revolving wings. I". *J. Exp. Biol.* 205, 15471564.; 2002
- [11] Walker, J. A., "Rotational lift: something different or more of the same?". *Journal of Experimental Biology*, 205, 3783-3792; 2002.
- [12] Wang, Z. J. "Passive wing pitch reversal in insect flight". *J. Fluid Mech*, vol 591, pp. 321-337.; 2007
- [13] Wood, R. J. "The First Takeoff of a Biologically Inspired At-Scale Robotic Insect". *IEEE TRANSACTIONS ON ROBOTICS*, VOL. 24, NO. 2, APRIL 2008
- [14] Wootton, R. J, "Functional Morphology of insect wings". *Annu. Rev. Entomol.* 37:113-40.; 1992